



## 1 **The characteristics of the 2022 Tonga volcanic tsunami in** 2 **the Pacific Ocean**

3 Gui Hu<sup>1</sup>, Linlin Li<sup>1,2</sup>, Zhiyuan Ren<sup>3</sup>, Kan Zhang<sup>1</sup>

4 1. Guangdong Provincial Key Laboratory of Geodynamics and Geohazards, School of Earth Sciences  
5 and Engineering, Sun Yat-sen University, Guangzhou, China

6 2. Southern Marine Science and Engineering Guangdong Laboratory (Zhuhai), Zhuhai, China

7 3. Department of Civil and Environmental Engineering, National University of Singapore, Singapore.

8 *Correspondence to:* Linlin Li (lilinlin3@mail.sysu.edu.cn)

9 **Abstract.** On 15th January 2022, an exceptional eruption of Hunga Tonga–Hunga Ha’apai volcano  
10 generated atmospheric and tsunami waves that were widely observed at oceans globally, gaining a  
11 remarkable attention to scientists in related fields. The tsunamigenic mechanism of this rare event  
12 remains an enigmatic due to its complexity and lacking of direct underwater observations. Here, to  
13 explore the tsunamigenic mechanisms of this volcanic tsunami event and its hydrodynamic processes in  
14 the Pacific Ocean, we conduct tsunami waveform and spectral analyses of the waveform recordings at  
15 116 coastal gauges and 38 deep-ocean buoys across the Pacific Ocean. Combined with the constraints of  
16 some representative barometers, we obtain the plausible tsunamigenic origins during the volcano activity.  
17 We identify four distinct tsunami wave components generated by air-sea coupling and seafloor crustal  
18 deformation. Those tsunami components are differentiated by their different propagating speeds or period  
19 bands. The first-arriving tsunami component with ~80–100 min period was from shock waves spreading  
20 at a velocity of ~1000 m/s in the vicinity of the eruption. The second component with extraordinary  
21 tsunami amplitude in deep sea was from Lamb waves. The Lamb wave with ~30–40 min period radically  
22 propagated outward from the eruption site with spatially decreasing propagation velocities from ~340  
23 m/s to ~315m/s. The third component with ~10–30 min period was probably from some atmospheric  
24 gravity wave modes propagating faster than 200 m/s but slower than Lamb waves. The last component  
25 with ~3–5 min period originated from partial caldera collapse with dimension of ~0.8–1.8 km.  
26 Surprisingly, the 2022 Tonga volcanic tsunami produced long oscillation in the Pacific Ocean which is  
27 comparable with those of the 2011 Tohoku tsunami. We point out that the long oscillation is not only  
28 associated with the resonance effect with the atmospheric acoustic-gravity waves, but more importantly  
29 the interactions with local bathymetry. This rare event also calls for more attention to the tsunami hazards



30 produced by atypical tsunamigenic source, e.g., volcanic eruption.

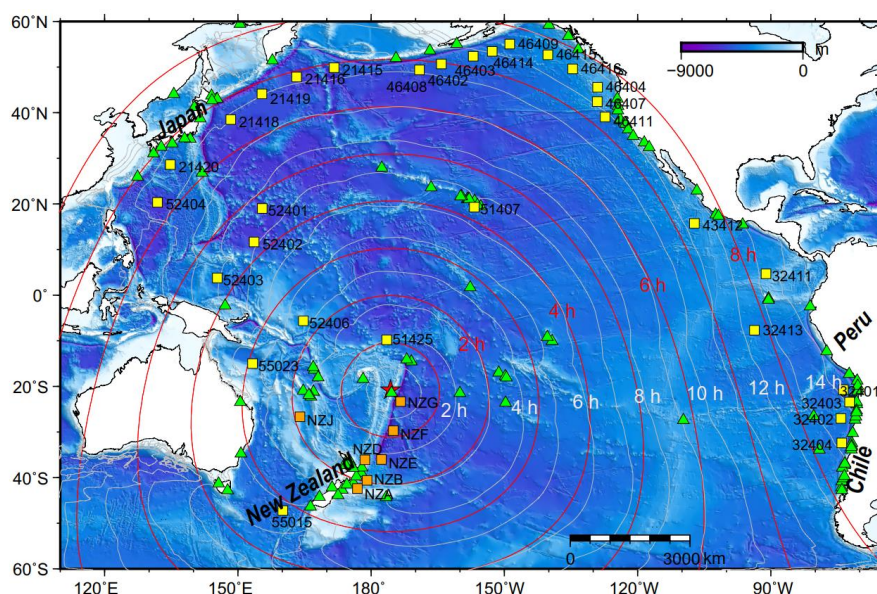
## 31 **1. Introduction**

32 On 15 January 2022 at 04:14:45 (UTC), a submarine volcano erupted violently at the uninhabited Hunga  
33 Tonga-Hunga Ha'apai (HTHH) island at 20.546°S 175.390°W (USGS, 2022). The volcano is located ~67  
34 km north of Nuku'alofa, the capital of Tonga (NASA, 2022) (Figure 1). The blasts launched plumes of  
35 ash, steam, and gas ~58 km high into stratosphere (Yuen et al., 2022) which not only blanketed nearby  
36 islands in ash (Duncombe, 2022; NASA, 2022), but caused various atmospheric acoustic-gravity wave  
37 modes (AGWs) of various scales, e.g., Lamb waves from atmospheric surface pressure disturbance  
38 associated with the eruption (Liu and Higuera, 2022; Adam, 2022; Kubota et al., 2022; Matoza et al.,  
39 2022). Tsunami with conspicuous sea level changes were detected by coastal tide gauges and Deep-ocean  
40 Assessment and Reporting of Tsunamis (DART) buoy stations in the Pacific (Figure 1), the Atlantic, and  
41 Indian Oceans as well as the Caribbean and Mediterranean seas (Carvajal et al., 2022; Kubota et al., 2022;  
42 Ramírez-Herrera et al., 2022), while the large waves were mainly concentrated in the Pacific Ocean, like  
43 coastlines of New Zealand, Japan, California, and Chile (Carvajal et al., 2022). The event caused at least  
44 3 fatalities in Tonga. Two people drowned in northern Peru when ~2 m destructive tsunami waves  
45 inundated an island in the Lambayeque region, Chile (Edmonds, 2022).

46 Satellite images revealed that the elevation of HTHH island has gone through dramatic change before  
47 and after the mid-January 2022 eruption. Previously, after the 2015 eruption, the two existing Hunga  
48 Tonga and Hunga Ha'apai Islands were linked together. The volcanic island rose 1.8 km from the seafloor  
49 where it stretched ~20 km across and topped a underwater caldera ~5 km in diameter (Garvin et al., 2018;  
50 NASA, 2022). After the violent explosion on 15 January 2022, the newly formed island during 2015 was  
51 completely gone, with only small tips left in far southwestern and northeastern HTHH island (NASA,  
52 2022). HTHH volcano lies along the northern part of Tonga–Kermadec arc, where the Pacific Plate  
53 subducts under the Indo-Australian Plate (Billen et al., 2003). The convergence rate (15–24 cm/year)  
54 between the Tonga-Kermadec subduction system and the Pacific plate is among the fastest recorded plate  
55 velocity on Earth, forming the second deepest trench around the globe (Satake, 2010; Bevis et al., 1995).  
56 The fast convergence rate contributes to the frequent earthquakes, tsunamis and volcanic eruptions in  
57 this region historically (Bevis et al., 1995). The 2022 HTHH volcano is part of a submarine-volcano



58 chain that extends all the way from New Zealand to Fiji (Plank et al., 2020). HTHH volcano had many  
59 notable eruptions before 2022 since its first historically recorded eruption in 1912, i.e., in 1937, 1988,  
60 2009, 2014-2015 (Global Volcanism Program, <https://volcano.si.edu>).



61  
62 **Figure 1.** The spatial distribution of the eruption site (red star), DART stations (squares), tide gauges  
63 (triangles) and the calculated tsunami arrival times. White contours indicate the modelled arrival times of  
64 conventional tsunamis. Red contours indicate the estimated arrival times of Lamb waves (see how we derive  
65 these contours in section 3.1).

66 The 2022 HTHH eruption is the first volcanic event which generates worldwide tsunami signatures since  
67 the 1883 Krakatau event (Matoza et al., 2022; Self and Rampino, 1981; Nomanbhoy and Satake, 1995).  
68 The tsunamigenic mechanism of this rare volcanic eruption-induced tsunami is still poorly understood  
69 due to its complex nature and the deficiencies of near-field seafloor surveys. Various tsunami generation  
70 mechanisms have been proposed so far based on the observations of ground-based and spaceborne  
71 geophysical instrumentations (Kubota et al., 2022; Matoza et al., 2022; Carvajal et al., 2022). The most-  
72 mentioned mechanism is the fast-traveling atmospheric Lamb wave generated by the atmospheric  
73 pressure rise of  $\sim 2$  hPa during the eruption. The Lamb wave circled the Earth for several times with  
74 travelling speed close to that of the sound wave in the lower atmosphere, leading to globally observed  
75 sea level fluctuations (Adam, 2022; Duncombe, 2022; Kubota et al., 2022; Matoza et al., 2022) (Figure  
76 1). The second mechanism is suggested to be a variety of other acoustic-gravity wave modes (Adam,  
77 2022; Matoza et al., 2022; Themens et al., 2022; Zhang et al., 2022). The third mechanism may be related



78 to the seafloor crustal deformation induced by one or more volcanic activities in the vicinity of the  
79 eruption site (e.g., pyroclastic flows, partial collapse of the caldera) (Carvajal et al., 2022) , which are  
80 more responsible for the near-field tsunamis with theoretical tsunami speeds.

81 To investigate the possible tsunamigenic mechanisms and detailed hydrodynamic behaviors of this rare  
82 volcanic tsunami event, in this study, we collect, process and analyze the sea level measurements from  
83 116 tide gauge and 38 DART buoys in the Pacific Ocean (shown in Figures 1 and 2). We first do statistical  
84 analysis of the tsunami waveforms to estimate the propagating speed of the Lamb wave and to understand  
85 the tsunami wave characteristics in the Pacific Ocean through demonstrating the tsunami wave properties,  
86 i.e., arrival times, wave heights and durations. We then conduct wavelet analysis for representative DART  
87 buoys and tide gauges respectively to explore tsunamigenic mechanisms of the event and to better  
88 understand its hydrodynamic processes in the Pacific Ocean. Aided by wavelet analysis of corresponding  
89 barometers near the selected DART buoys and comparison with tsunami records of the 2011 Tohoku  
90 tsunami, we are able to piece together all the analysis and demonstrate that the 2022 HTHH tsunami was  
91 generated by air-sea coupling with a wide range of atmospheric waves with different propagating  
92 velocities and period bands, and seafloor crustal deformation associated with the volcanic eruption. We  
93 demonstrate as well that the tsunami was amplified at the far-field Pacific coastlines where the local  
94 bathymetric effects play a dominant role in tsunami scale.

## 95 **2. Data and Methods**

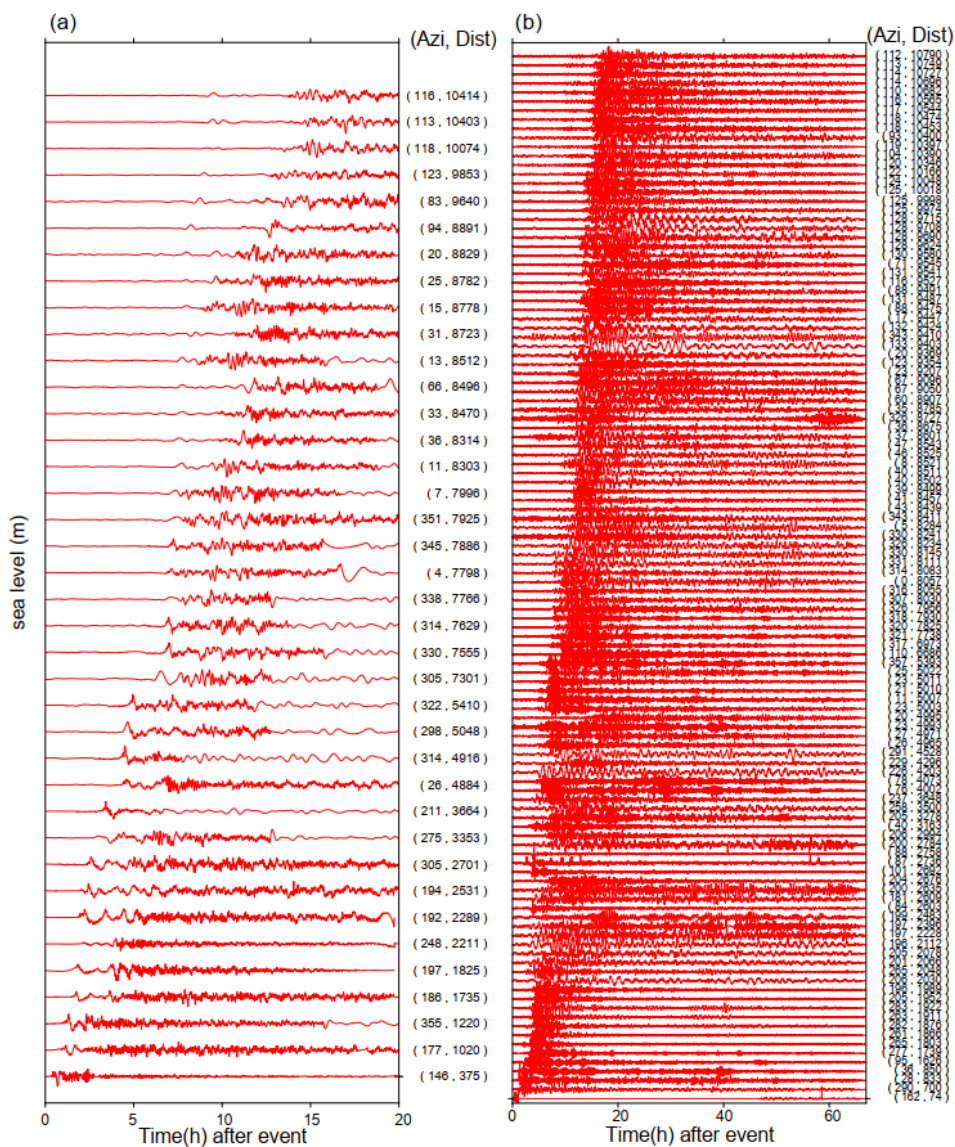
### 96 **2.1 Data**

97 We collected high-quality sea level records across the Pacific Ocean at 38 DART buoys (in which 31  
98 stations from <https://nctr.pmel.noaa.gov/Dart/>, 7 stations from <https://tilde.geonet.org.nz/dashboard/>) and  
99 116 tide gages from IOC (The Intergovernmental Oceanographic Commission, <http://www.ioc-sealevelmonitoring.org>) (Figure 1). The epicentral distances of tide gauges and DART buoys range  
100 between 74–10790 km and 375–10414 km, respectively. The sampling rates of DART buoys are  
101 changing over time. Passing of tsunami event generally can trigger the DART system to enter its high  
102 frequency sampling mode (15 seconds or 1 min) from normal frequency mode (15 min)  
103 ([www.ndbc.noaa.gov/dart](http://www.ndbc.noaa.gov/dart)). In contrast, sampling rates of normal tide gauges at coasts are uniform with  
104 sampling interval of 1 min. The sampling interval of both DART and tide gauges is preprocessed to 15  
105



106 seconds. Firstly, we eliminate abnormal spikes and fill gaps by linear interpolation. Secondly, we applied  
107 a fourth-order Butterworth-Highpass filter with a cut-off frequency of  $3.5 \times 10^{-5}$  Hz (~ 8 hours) to remove  
108 the tidal components (Figure 2) (Heidarzadeh and Satake, 2013). After the two steps, quality control step  
109 is conducted to select high-quality data, in which we delete waveforms with spoiled data or massive data  
110 loss due to equipment failure, or with the maximum tsunami heights less than 0.2 m, then the selected  
111 data will be ready for further statistics and spectral analysis. We also collect and analyze the atmospheric  
112 pressure disturbance data recorded by some representative barometers. The sampling rates of the  
113 barometers is generally uniform with a sampling rate of 1 min except for some stations in New Zealand  
114 with interval of 10 min. Considering the sample rate, we employ a fourth-order Butterworth-Bandpass  
115 filter with period ranging between 2–150 min for wavelet analysis of the barometers with 1 min sample  
116 rate, while we apply the fourth-order Butterworth-Bandpass filter with range of 30–150 min to long-  
117 period waveform display based on two reasons. (1) The barometer data we use for the analysis include  
118 some in New Zealand with 10 min sample rate; (2) Filtering out the short-period waves helps highlight  
119 long-period tsunami wave components.

120 The tsunami waveforms recorded by DART buoys which are installed offshore in the deep water are  
121 expected to contain certain characteristics of the tsunami source (Wang et al., 2020, 2021). The  
122 waveforms recorded by tide gauge distributed along coastlines are significantly influenced by local  
123 bathymetry/topography which are used for investigating bathymetric effect on tsunami behaviors  
124 (Rabinovich et al., 2017, 2006; Rabinovich, 2009). Therefore, we use the DART data for source-related  
125 analysis and choose some tide gauge data to investigate the tsunami behaviors at the Pacific coastlines.



126

127

128

**Figure 2.** Detided tsunami waveforms at (a) DART buoys and (b) tide gauges. Waveforms in both subplots are shown in ascending distance.

129

## 2.2 Tsunami Modelling

130

131

132

133

We use a numerical tsunami modelling package JAGURS (Baba et al. 2015) to simulate the tsunami propagation of the 2022 HTHH event and obtain the theoretical tsunami arrival time based on the shallow water wave speed (white contours in Figure 1). The code solves linear Boussinesq-type equations in a spherical coordinate system using a finite difference approximation with the leapfrog method. We specify



134 a unit Gaussian-shaped vertical sea surface displacement at the volcanic base as the source of  
135 conventional tsunamis. For a unit source  $i$  with center at longitude  $\varphi_i$  and latitude  $\theta_i$ , the  
136 displacement distribution  $Z_i(\varphi, \theta)$  can be expressed as:

$$137 \quad Z_i(\varphi, \theta) = \exp\left[-\frac{(\varphi-\varphi_i)^2+(\theta-\theta_i)^2}{2\sigma}\right] \quad (1)$$

138 Where we set characteristic length  $\sigma$  as 5 km (NASA, 2022). The bathymetric data is resampled from the  
139 GEBCO 2019 with 15 arc-sec resolution (The General Bathymetric Chart of the Oceans, downloaded  
140 from <https://www.gebco.net>).

### 141 2.3 Spectral Analysis of Tsunami Waves

142 To investigate the temporal changes of the dominant wave periods, we conduct continuous wavelet  
143 transformation (frequency-time) analyses for some representative DART buoys, tide gauges and  
144 barometers, in which wavelet Morlet mother function is implemented (Kristeková et al., 2006). The first  
145 32-hour time series of DART buoys and barometers after the eruption (at 04:14:45 on 15 January 2022)  
146 are used for source-related wavelet analysis. The first 48-hour time series of tide gauges after the eruption  
147 are employed for hydrodynamics-related wavelet analysis at coastlines. We adopt the Averaged-Root-  
148 Mean-Square (ARMS) method as a measure of absolute average tsunami amplitude with a moving time  
149 window of 20 min to calculate the tsunami duration (Heidarzadeh and Satake, 2014). We define the time  
150 durations as the time period where ARMS levels of tsunami waves are above those prior to the tsunami  
151 arrivals.

## 152 3. Results

### 153 3.1 The decreasing propagation velocities of the Lamb Wave

154 Although many types of atmospheric waves were generated by the 2022 HTHH eruption, the most  
155 prominent signature was the Lamb waves which were globally observed by ground-based and spaceborne  
156 geophysical instrumentations (Kulichkov et al., 2022; Liu et al., 2022; Lin et al., 2022; Matoza et al.,  
157 2022; Themens et al., 2022; Adam, 2022; Kubota et al., 2022). Interestingly, we notice that a wide range  
158 of the velocities from 280 m/s to 340 m/s were proposed through observations and Lamb wave modelling  
159 (e.g., Kubota et al., 2022; Lin et al., 2022; Matoza et al., 2022; Themens et al., 2022). The travelling  
160 velocity of Lamb waves in real atmosphere is affected by temperature distributions, winds and dissipation

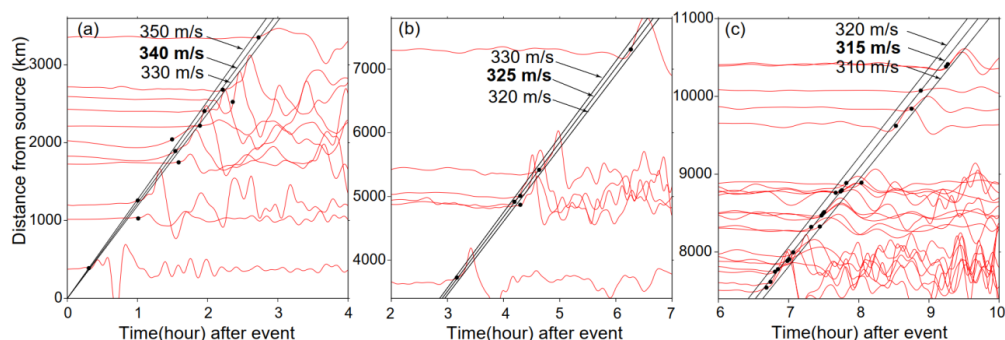


161 (Otsuka, 2022). To investigate whether the propagation speeds of the lamb wave change in space and  
162 time, we analyze the waveforms recorded by the DART buoys in the Pacific Ocean. The Pacific DART  
163 buoys recorded the most discernible air-sea coupling pulse in deep ocean with Lamb waves that arrived  
164 earlier than the theoretical tsunamis (Figure 1). The tsunami waveforms recorded by tide gauges did not  
165 clearly detect the tsunami signals associated with the lamb waves, therefore not sufficient for further  
166 analysis (Figure 2). Thus, we estimate the speed of Lamb waves using the waveforms recorded by the  
167 Pacific DART buoys. The Lamb wave arrivals are limited within arrival time range from possible  
168 velocities of 280–340 m/s. The time points at which the tsunami amplitudes first exceed 1 e-4 m above  
169 sea level are defined as Lamb wave arrivals. By carefully fitting the arrivals with different constant  
170 velocities, we illustrate the velocities of Lamb wave were generally uniform, but slightly decrease with  
171 the increase of propagation distance (Figure 3). The Lamb waves initially propagated radially at speed  
172 of ~340 m/s before slowing to ~325 m/s after reaching ~3400 km, and further decreasing to ~315 m/s at  
173 7400 km. In an isothermal troposphere assumption, the phase velocity of the Lamb wave ( $C_L$ ) can be  
174 estimated with the following equation (Gossard and Hooke, 1975):

$$175 \quad C_L = \sqrt{\frac{\gamma R T}{M}} \quad (2)$$

176 Where  $\gamma = 1.4$  (air specific heat ratio corresponding to atmospheric temperature),  $R = 8314.36 \text{ J kmol}^{-1}$   
177  $\text{K}^{-1}$  (the universal gas constant),  $M = 28.966 \text{ kg kmol}^{-1}$  (molecular mass for dry air) are constant for the  
178 air,  $T$  is the absolute temperature in kelvin. Thus, Lamb wave velocity is mainly affected by the air  
179 temperature, meaning the travelling velocity of lamb waves might decrease when propagating from  
180 regions with high temperature towards those with low temperatures, e.g., the north pole. By assuming a  
181 set of possible temperatures in January (Table 1), we calculated the velocities  $C_L$  could range between  
182 312–343 m/s when temperatures vary between -30–20 °C. Therefore, the decreased velocity of the lamb  
183 waves could be a consequence of cooling of the air temperature.





184  
 185 **Figure 3. Fitting the arrival times of normalized Lamb waveforms with different velocities. Black dots mark**  
 186 **the arrival times of the Lamb waves. Black lines represent velocities.**

187 **Table 1. Estimated Lamb wave velocities in an isothermal troposphere assumption**

Celsius temperature (°C)	thermodynamic temperature (K)	$C_L$ (m/s)
20	293.15	343.14
10	283.15	337.23
0	273.15	331.21
-10	263.15	325.19
-20	253.15	318.86
-30	243.15	312.49

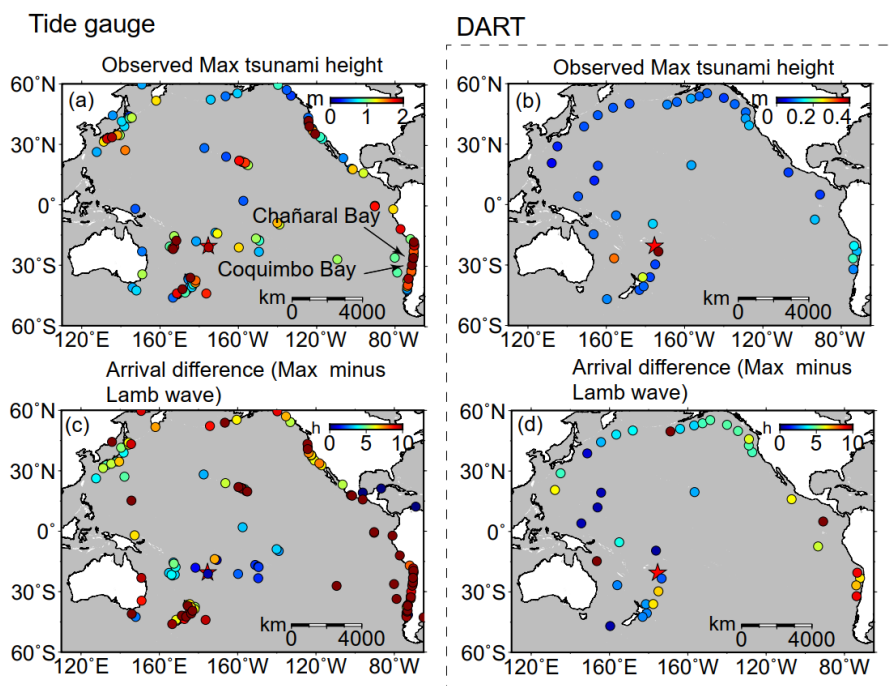
188 **3.2 Tsunami features observed by DART buoys and Tide gauges**

189 The statistics of tsunami heights and arrival times recorded at 38 DART buoys and 116 tide gauges across  
 190 the Pacific Ocean are used to interpret the tsunami characteristics. The comparison of the statistical  
 191 characters between DART and tide gauge observations yields some useful information of the  
 192 hydrodynamic process of tsunami propagation and help identify tsunami wave components with different  
 193 traveling velocities.

194 The average value of the maximum tsunami wave height (trough-to-crest) for the 116 tide gauge stations  
 195 is ~1.2 m. Figure 4a shows tide gauges with large tsunami heights exceeding 2 m are mainly distributed  
 196 in coastlines with complex geometries, such as gauges at New Zealand, Japan, and north and south  
 197 America. For example, the largest tsunami height among tide gauges is 3.6 m at a bay-shaped coastal  
 198 area Chañaral in Chile. In sharp contrast to tide gauges, the maximum tsunami heights of most Pacific  
 199 DART buoys are less than 0.2 m. The largest tsunami height in the DART buoys is only ~0.4 m recorded  
 200 at the nearest one, 375 km from the volcano (Figure 4b). The comparison between DART buoys and tide  
 201 gauges indicate that the direct contribution of air-sea coupling to the tsunami heights is probably in the



202 level of tens of centimeters (Kubota et al., 2022). The meter-scale tsunami heights at the coastlines  
203 suggest the bathymetric effect could play a major role during tsunami propagation. In respect to the  
204 arrival of maximum tsunami waves, the time lags between Lamb waves and the maximum heights of tide  
205 gauges mainly range between ~0–10 h (Figure 4c). The delayed times of ~10 h are observed in New  
206 Zealand, Hawaii, and west coast of America (Figure 4c), suggesting the interaction between tsunami  
207 waves and local topography/bathymetry delay the arrival of the maximum waves (e.g., Hu et al., 2022).  
208 The significant regional dependence of the coastal tsunami heights and the time lags of the maximum  
209 tsunami waves can be attributed to the complexity of local bathymetry, such as continental shelves with  
210 different slopes, and harbor/bay with different shapes and sizes (Satake et al., 2020). On the other hand,  
211 since the DART records are less influenced by bathymetric variation in space, the first waves in DART  
212 buoys are supposed to be the maximum tsunami waves as observed in the 2011 Tohoku tsunami event  
213 (Heidarzadeh and Satake, 2013). However, we observe the inconsistency between the arrivals of the  
214 Lamb waves and the maximum tsunami heights (Figure 4d). The time lags of the maximum waves of  
215 DART buoys present a coarsely increasing tendency with the increasing distance from the volcano, which  
216 indicates the contribution of other tsunami generation mechanism propagating with a uniform but lower  
217 speed than Lamb wave.



218

219

220

221

222

223

224

225

226

227

228

229

230

231

232

233

234

**Figure 4.** The spatiotemporal signatures of the 2022 HTHH tsunami across the Pacific Ocean. (a) Observed the maximum tsunami height (trough-to-crest height) of tide gauges. (c) Arrival differences between the maximum tsunami height of tide gauges and Lamb waves. (b) and (d) are the same as (a) and (c) but for DART buoys.

### 3.3 Tsunami components identified from wavelet analysis

The statistical analysis of tsunami waveforms at tide gauges and DART buoys suggest the tsunami waves likely contain several components with different source origins. To further identify these tsunami components, we conduct wavelet analysis for tsunami waveforms recorded by representative DART buoys and air pressure waveforms recorded by selected barometers. We demonstrate the analysis result through the frequency-time (f-t) plot of wavelet which shows how energy and period vary at frequency and time bands (Figure 5 and Figure 6). Tsunami components have clear signatures in all f-t plots as the energy levels are quite large when they arrive. Figure 5 shows the wavelet analysis of six DART buoys located in the vicinity of the eruption site (<3664 km). Figure 6 show the wavelet analysis of ten DART buoys located in the Pacific rim which are far away from the source location. We observe three interesting phenomena: 1) most of the tsunami wave energy is concentrated in four major period bands, i.e., ~80–100 min, 10–30 min, 30–40 min, and 3–5 min; 2) The stations with 3-5 mins wave periods are mainly



235 located in the vicinity of the volcano site; 3) There exist one exceptional tsunami component with longer  
236 wave period of ~80–100 min in the near source region which travels even faster than the Lamb waves.  
237 To further explore the source mechanism of these tsunami components, we take advantage of the  
238 published information related to different propagating velocities of atmospheric gravity waves (Kubota  
239 et al., 2022) and add four kinds of propagating velocities as criteria to differentiate the tsunami arrivals  
240 from different sources (Figure 5 and Figure 6). The first reference speed is 1000 m/s related to the  
241 radically propagating atmospheric shock waves near the source region (Matoza et al., 2022; Themens et  
242 al., 2022). The second one is the velocities of Lamb wave ranging between 315–340 m/s derived from  
243 the aforementioned analysis in section 3.1 (Figure 3). The third one is 200 m/s corresponding to the lower  
244 limit of atmospheric gravity wave modes other than Lamb waves which were also excited by the volcanic  
245 eruptions (Kubota et al., 2022). The last is the arrival time of conventional tsunami given by tsunami  
246 modelling (Figure 1). The theoretical velocity of conventional tsunami is significantly nonuniform  
247 spatially as compared with those of the atmospheric waves. The conventional tsunami propagation speed  
248 is determined by the water depth along the propagation route. The velocity of non-dispersion shallow-  
249 water waves ( $C_H$ ) in the ocean is given by:

$$250 \quad C_H = \sqrt{g \cdot H} \quad (3)$$

251 Where  $g$  is gravity acceleration ( $9.81\text{m/s}^2$ ),  $H$  is the water depth. The propagation velocities of tsunami  
252 are ~296–328 m/s in the deepest trenches on earth (i.e., ~11 km in Mariana Trench and ~9 km in Tonga  
253 Trench). The velocities decrease quickly to only ~44 m/s at ~200 m depth along the edge of continental  
254 shelf. With the average depth of ~4–5 km, the average velocities in the Pacific Ocean range between  
255 ~198–221 m/s. Thus, theoretical tsunami velocities present significant slowness and variability. We  
256 delineate the arrival times of the four reference speeds in Figures 5 and 6. For each panel of the figures,  
257 from left to right, the solid vertical white lines mark velocity of 1000 m/s. The solid vertical red lines  
258 mark the arrival of Lamb waves. The dashed vertical white lines mark lower limit of gravity waves'  
259 velocity of 200 m/s. The dashed vertical black lines represent the calculated theoretical tsunami arrivals.  
260 Horizontal white dashed lines mark two reference periods of 10 min and 30 min.

261 One particularly remarkable phenomenon is that the wave component with period of ~80–100 min  
262 propagated at a very fast speed of ~1000 m/s in the vicinity of the HTHH site, i.e., New Zealand and  
263 Hawaii (e.g., stations 52406, NZJ, NZE, 51425 in Figure 5). We infer that the tsunami component within



264 ~80–100 min period band was likely produced by the atmospheric shock waves during the initial stage  
265 of the volcanic eruption and spatially only cover the near-source region. To verify this observation, we  
266 select 16 representative barometers located in the near-source region and far-field area for wavelet  
267 analysis (see the locations in Figure 5 and Figure 6). Figure 7 shows the waveforms of atmospheric  
268 pressure at selected locations and Figure 8 provides the frequency-time (f-t) plot of wavelet analysis of  
269 some representative barometers. Interestingly, we are able to discern the air pressure pulses prior to Lamb  
270 waves at barometers in New Zealand (the two columns on the left in Figure 7), although such signals are  
271 not detectable in waveforms recorded by barometers far from the source (the two columns on the right  
272 in Figure 7). The spatial distribution of such unusual pressure changes suggest that the fast travelling  
273 shock waves were only limited in the near-source region, as reflected in the travelling ionospheric  
274 disturbances (Matoza et al., 2022; Themens et al., 2022). Additionally, we also see that the long period  
275 signals of ~80–100 min appear in DART buoys far away from the eruption site. Such signals may be  
276 related with the long-period gravity waves (Matoza et al., 2022).

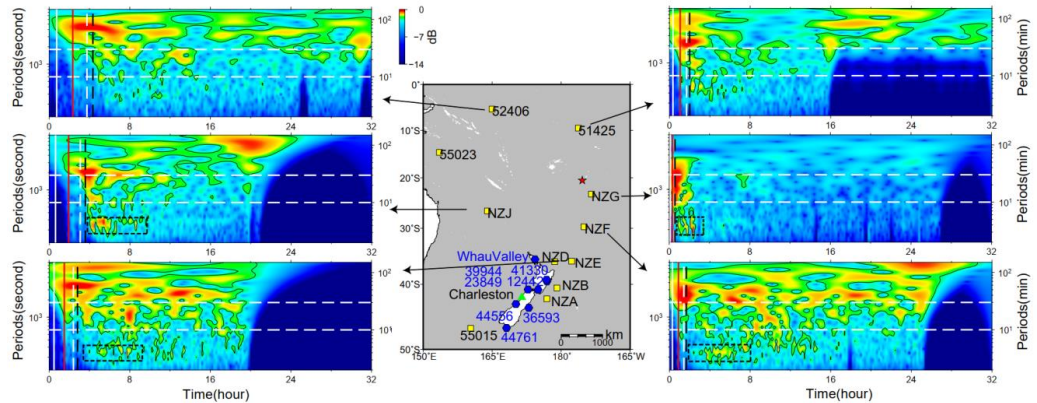
277 The tsunami components at period band of ~30–40 min can be readily associated with Lamb waves  
278 because the arrival times of tsunami waves and Lamb waves have excellent match, as shown in the  
279 tsunami data recorded by DART buoys (e.g., NZJ and 51425 in Figure 5; 51407, 32401 and 32413 in  
280 Figure 6) and pressure data by barometers (Figure 8).

281 For the tsunami components with the period band of ~10–30 min, although the arrivals of ~10–30 min  
282 tsunami components cover some theoretical tsunami arrival times, they do not consistently match. The  
283 tsunami components occurring within the time period between Lamb waves and the lower gravity waves'  
284 velocities has a good agreement with the velocity range of several atmospheric gravity wave modes  
285 (Matoza et al., 2022; Themens et al., 2022; Kubota et al., 2022). Similarly, the air pressure data also show  
286 energy peaks at ~10–30 min period band, which is consistent with the tsunami data (Figure 8). Such  
287 consistency further verifies the contribution of atmospheric gravity waves to the volcanic tsunami.

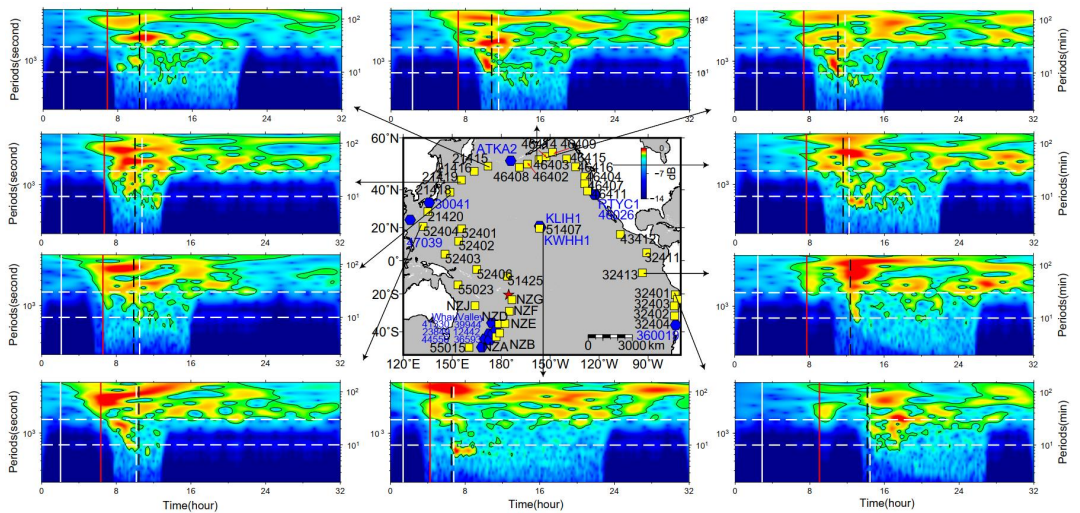
288 The tsunami components with the shortest period of ~3–5 min (stations NZE, NZF, NZG and NZJ;  
289 marked with black dashed squares in Figure 5) are only observed at DART records near the eruption  
290 location. Meanwhile, the arrival times of these components agree well with the modelled arrivals of  
291 conventional tsunami. Thus, we believe the observed shortest period band should originate from the  
292 seafloor crustal deformation. We further infer that this component could be generated by the partial



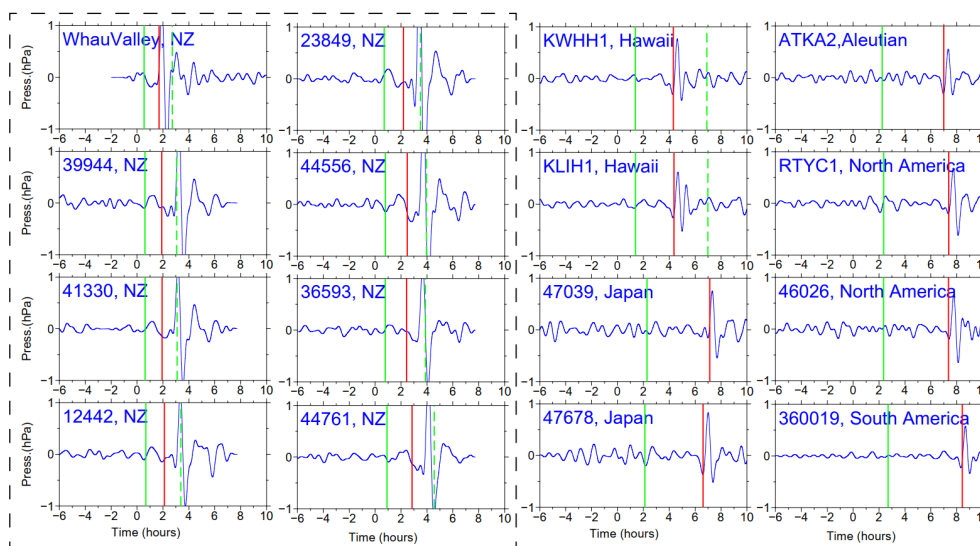
293 underwater caldera collapse and/or subaerial/submarine landslide failures associated with 2022 HTHH  
 294 volcanic eruption.



295  
 296 **Figure 5.** Wavelet analysis of representative DART buoys in the vicinity of the HTHH volcano. In each sub-  
 297 plot, the solid vertical white lines mark the arrival time with travelling velocity of 1000 m/s. The solid vertical  
 298 red lines mark the arrivals of Lamb waves. The dashed vertical white lines mark lower limit of AGWs' velocity  
 299 of 200 m/s (Kubota et al., 2022). The dashed vertical black lines represent the theoretical tsunami arrivals.  
 300 The dashed horizontal white lines mark two reference wave periods of 10 min and 30 min. The blue hexagons  
 301 represent the locations of barometers. Green triangle makes the location of the tide gauges at Charleston.

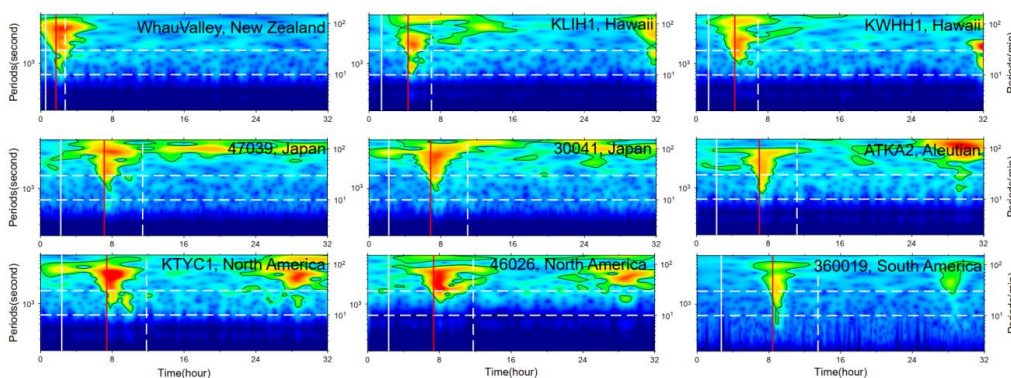


302  
 303 **Figure 6.** Wavelet analysis of representative DART buoys far away from the HTHH volcano. In each sub-  
 304 plot, the solid vertical white lines mark the arrival time with travelling velocity of 1000 m/s. The solid vertical red  
 305 lines mark the arrivals of Lamb waves. The dashed vertical white lines mark lower limit of AGWs' velocity  
 306 of 200 m/s. The dashed vertical black lines represent the theoretical tsunami arrivals. The dashed horizontal  
 307 white lines mark two reference wave periods of 10 min and 30 min. The blue hexagons represent the locations  
 308 of barometers.



309

310 **Figure 7. Shockwave-related atmospheric pressure waveforms of selected barometers in the Pacific Ocean.**  
 311 **All traces have been filtered between 30 min and 150 min. In each sub-plot, the solid vertical green lines mark**  
 312 **the arrival time with travelling velocity of 1000 m/s. The solid vertical red lines mark the arrivals of Lamb**  
 313 **waves. The dashed vertical green lines mark lower limit of AGWs' velocity of 200 m/s.**



314

315 **Figure 8. Wavelet analysis of some representative barometers. In each sub-plot, the solid vertical white lines**  
 316 **mark the arrival time with travelling velocity of 1000 m/s. The solid vertical red lines mark the arrivals of**  
 317 **Lamb waves. The dashed vertical white lines mark lower limit of AGWs' velocity 200 m/s. The dashed**  
 318 **horizontal white lines mark three reference periods of 10 min and 30 min.**

## 319 4. Discussion

### 320 4.1 Tsunami from Caldera Collapse and Its Long-distance Traveling Capability

321 The tsunami wave energy distributed in different period bands is identified with reference arrival times.

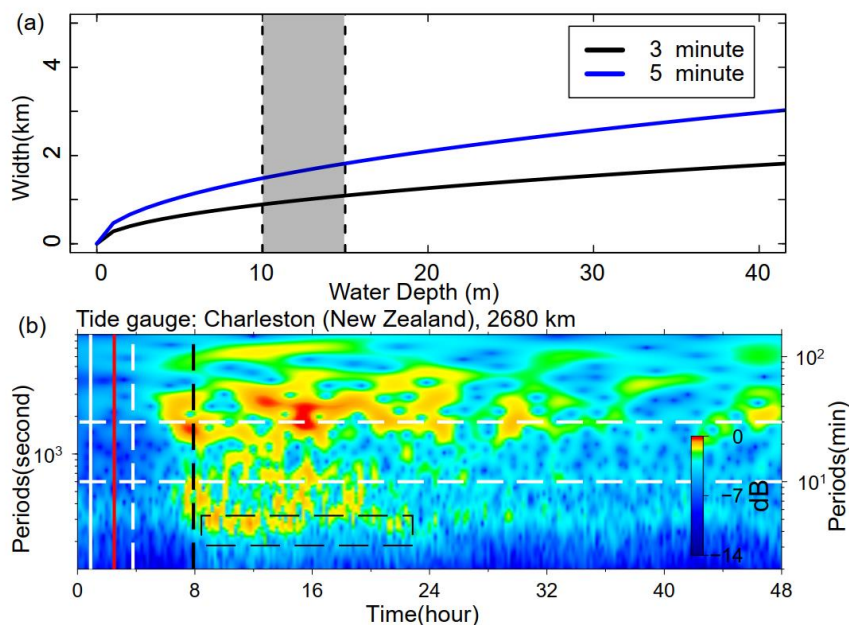


322 The tsunami component with 3–5 min period is most likely generated by seafloor crustal deformation in  
323 the volcanic site, but specific mechanism is not determined. A variety of possible scenarios associated  
324 with the eruption could be responsible for the near-field tsunami waves, such as volcanic earthquakes,  
325 pyroclastic flows entering the sea, underwater caldera flank collapse, and subaerial/submarine failures  
326 (Self and Rampino, 1981; Pelinovsky et al., 2005). To further investigate the source mechanism, we  
327 apply a simplified model to estimate the probable dimension of tsunami source:

$$328 \quad L = \frac{T\sqrt{gH}}{2} \quad (4)$$

329 Where  $L$  is the typical dimension (length or width) of the tsunami source,  $H$  is average water depth in the  
330 source area,  $g$  is the gravity acceleration, and  $T$  is primary tsunami period. By comparing with the post-  
331 2015 morphology of the HTHH caldera which was obtained through drone photogrammetry and  
332 multibeam sounder surveys, Stern et al. (2022) estimate that much of the newly-formed Hunga Tonga  
333 Island and the 2014/2015 cone were destroyed by the 2022 eruption, and the vertical deformation of  
334 Hunga Ha’apai Island is ~10–15 m (Stern et al., 2022). With no more quantitative constraint of the  
335 seafloor deformation, we tentatively assume  $H$  as 10–15 m, then the possible dimension of seafloor  
336 crustal deformation responsible for the small-scale tsunami could be in the scale of 0.8–1.8 km (Figure  
337 9a). The estimated size is very likely from partial caldera collapse that usually has limited scale in  
338 volcanic site (Ramalho et al., 2015; Omira et al., 2022). If it is the case, the partial flank collapse could  
339 be located between Hunga Tonga and Hunga Ha’apai Islands.





340

341 **Figure 9. Mechanism of tsunami component with 3–5min period. (a) The source dimension estimated by**  
342 **equation 4. (b) Wavelet analysis of tide gauge at Charleston, New Zealand, 2680 km away from the eruption**  
343 **site. The solid vertical white line marks the arrival time with travelling velocity of 1000 m/s. The solid vertical**  
344 **red line marks the arrival of Lamb wave. The dashed vertical white line marks lower limit of AGWs' velocity**  
345 **200 m/s. The dashed vertical black line marks the theoretical tsunami arrivals.**

346 An interesting phenomenon is that the tsunami component with 3–5 min period can still be observed in  
347 a bay-shaped coastal area at Charleston in New Zealand (see the location in Figure 5) which is 2680 km  
348 away from the eruption site and maintains a high energy level lasting up to 14 h (Figure 9b). The long-  
349 traveling capability could be associated with the ~ 10000 m deep water depth of the Tonga Trench that  
350 keeps the source signals from substantial attenuation. In deep open ocean, the wavelength of a tsunami  
351 can reach two hundred kilometers, but the height of the tsunami may be only a few centimeters. Tsunami  
352 waves in the deep ocean can travel thousands of kilometers at high speeds, meanwhile losing very little  
353 energy in the process. The long oscillation can be attributed to the multiple reflections of the incoming  
354 waves trapped in the shallow-water bay at Charleston.

355 Generally, devastating tsunamis with long-distance travelling capability are mostly generated by  
356 megathrust earthquakes (Titov et al., 2005). Caldera collapses or submarine landslides with limited scale  
357 normally only generate local tsunamis, e.g., the 1998 PNG (Papua New Guinea) tsunami event (Kawata



358 et al., 1999) and the 1930 Cabo Girão tsunami event (Ramalho et al., 2015). Therefore, it's exceptional  
359 that the tsunami component from scale-limited failure could travel at-least 2680 km away from the  
360 eruption site. It demonstrates that tsunamis from small-scale tsunamigenic source have the capability to  
361 travel long distance and cause long oscillation at favored condition, e.g., deep trench, ocean ridge and  
362 bay-shaped coasts.

#### 363 **4.2 The Possible Mechanisms of Long Tsunami Oscillation**

364 An important tsunami behavior of the 2022 HTHH tsunami is the long-lasting oscillation ~ 3 days in the  
365 Pacific Ocean (Figure 10a), which is comparable to that of the 2011 Tohoku tsunami, ~4 days  
366 (Heidarzadeh and Satake, 2013). We demonstrate the duration time of the tsunami oscillation through  
367 ARMS (Averaged-Root-Mean-Square) approach that is a measure of absolute average tsunami amplitude  
368 in a time period. The long-lasting tsunami energy can be observed at many regions, such as the coasts of  
369 New Zealand, Japan, Aleutian, Chile, Hawaii, and west coasts of America. Several mechanisms could  
370 account for the long-lasting tsunami, including (1) Lamb waves circling the Earth multiple times  
371 (Amores et al., 2022; Matoza et al., 2022), (2) resonance effect between ocean waves and atmospheric  
372 waves (Kubota et al., 2022), and (3) bathymetric effect. We discuss the contribution of each mechanism  
373 in the following section.

374 To investigate the contribution of Lamb wave to the long-lasting tsunami, we compare the air pressure  
375 disturbances recorded by selected barometers together with the tsunami waveforms of nearby tide gauges  
376 (Figure 10b). While the barometers present discernible wave pulses at each Lamb wave's arrival, only  
377 the first Lamb wave triggered clear tsunami signal and no detectable tsunami signatures correspond to  
378 the following passage, suggesting the Lamb waves do not directly contribute to the long oscillation.

379 Theoretically, the resonance effects between ocean waves and atmospheric waves could contribute to the  
380 long oscillation on coastlines based on the following reasons. First, part of the atmospheric gravity waves  
381 propagated at velocities close to averaged velocities of conventional tsunami in the Pacific Ocean (198–  
382 221 m/s) which resulted in the resonance with ocean waves (Kubota et al., 2022). Second, in deep oceanic  
383 trenches, such as Mariana and Tonga-Kermadec trench (10000–11000 m), tsunami velocities range  
384 between ~314–330m/s which are comparable with those of the observed Lamb waves 315–340 m/s.  
385 When Lamb wave speed approaches the tsunami speed, Proudman resonance gradually increase tsunami  
386 heights, wherein Proudman resonance optimally maximizes tsunami heights when they match well



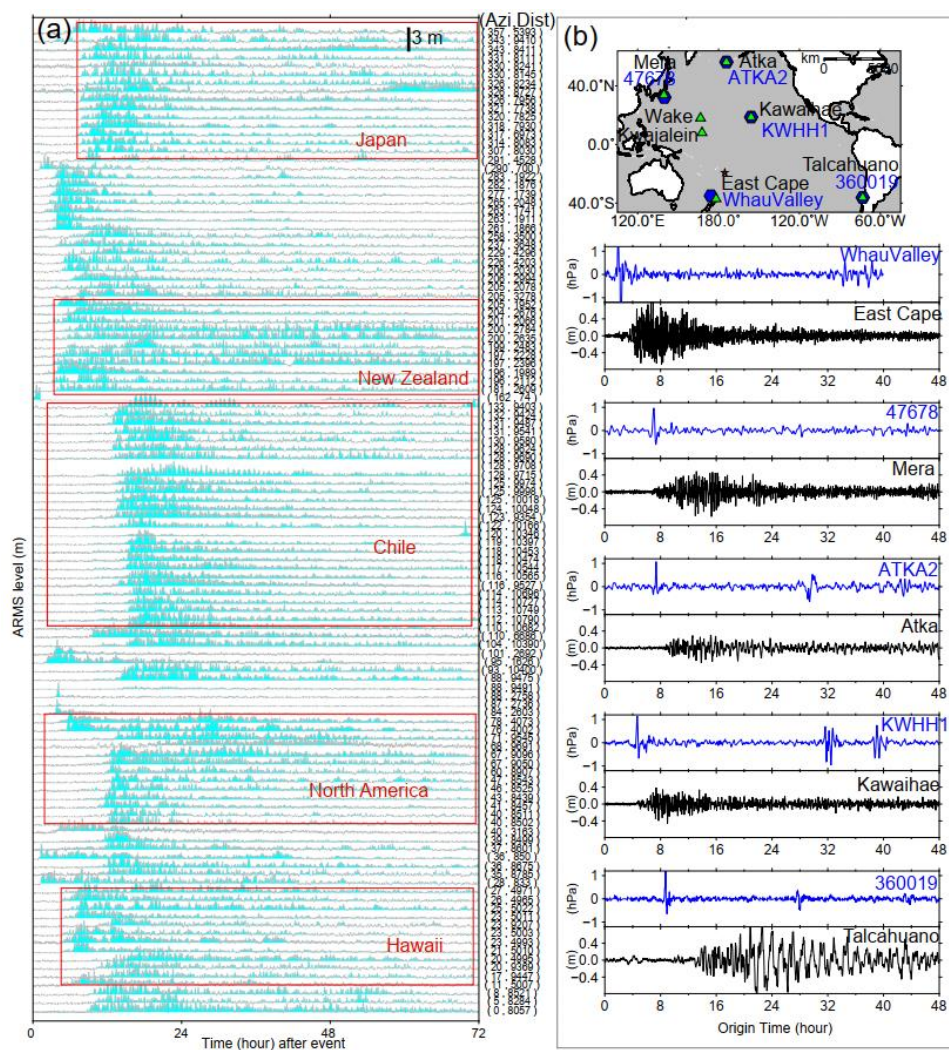
387 (Tanioka et al., 2022; Lynett et al., 2022). Therefore, the resonance effect continuously supplied wave  
388 energy to the ocean, especially in the deep trenches.

389 To examine the role of local bathymetry in the long-lasting tsunami, we choose a well-studied and well-  
390 recorded event: the 2011 Mw 9.0 Tohoku tsunami as a reference event and compare the tsunami records  
391 of these two events at the same coastal stations. Although the two tsunami events were generated by  
392 completely different mechanisms, i.e., large-scale seafloor deformation for the Mw 9.0 megathrust  
393 earthquake (Mori et al., 2011) and fast-moving atmospheric waves for the Mw 5.8 volcanic eruption  
394 (Titov et al., 2005), they both produced widespread transoceanic tsunamis which were well recorded in  
395 the Pacific DART buoys and tide gauges. In the near-field, the 2011 Tohoku earthquake produced runup  
396 up to 40 m at the Iwate Prefecture, ~70 km from the source (Tanioka et al., 2022), while the 2022 HTHH  
397 tsunami produced only ~13 m runup in the near field from eyewitness accounts in Kanokupolu, 60 km  
398 from the volcano (Lynett et al., 2022). However, in the far-field (>1000 km), we observe comparable  
399 tsunami wave heights in certain coastal regions. Based on the tsunami records at 21 tide gauges  
400 surrounding the Pacific Ocean, Heidarzadeh & Satake (2013) calculated the average value of the  
401 maximum tsunami heights (trough-to-crest) of the 2011 Tohoku tsunami is 1.6 m with the largest height  
402 of 3.9 m at the Coquimbo Bay in Chile (Heidarzadeh and Satake, 2013). Coincidentally, the statistics of  
403 116 tide gauges in this study also suggest the average tsunami heights of the 2022 HTHH tsunami is  
404 around the same order, ~1.2 m, among which, the largest height is 3.6 m at Chañaral Bay in Chile.  
405 Interestingly, in the coastal region of South America, the locations of the largest tsunami heights of both  
406 events are adjacent (Figure 4a), i.e., Coquimbo (the 2011 Tohoku) and Chañaral (The 2022 HTHH).

407 To further compare the far-field hydrodynamic processes between these two events quantitatively, we  
408 conduct wavelet analysis for four representative tide gauges distributed across the Pacific Ocean, i.e.  
409 coastal gauges at East Cape in New Zealand, Kwajalein Island, Wake Island, and Talcahuano in Chile  
410 (see their locations in Figures 10b). The temporal changes of tsunami energy of both events can be seen  
411 in Figure 11. At each tide gauge, the tsunami energy of the 2011 HTHH (Figure 11a) and the 2022 Tohoku  
412 tsunamis (Figure 11b) for the first few hours after the arrivals is nonuniform with different significant  
413 peaks distributed within a wide period band of ~3–100 min. Then, the following long-lasting energy of  
414 the both at each station presents similar pattern and is concentrated at identical and fairly narrower period  
415 channel, i.e., ~20–30 min at East Cape in New Zealand, ~40–60 min at Kwajalein Island, ~10 min at



416 Wake Island, and ~100 min at Talcahuaho in Chile, which reflects the local bathymetric effects of natural  
417 permanent oscillations (Hu et al., 2022; Satake et al., 2020). Specifically, many bathymetric effects can  
418 contribute to the long-lasting tsunami, such as multiple reflections across the basins, or the continental  
419 shelves, and the excited tsunami resonance in bays/harbors with variable shapes and sizes (Aranguiz et  
420 al., 2019; Satake et al., 2020). For example, tide gauges around New Zealand are primarily distributed in  
421 harbors/ports with major natural oscillation modes of ~20–30 min (De Lange and Healy, 1986; Lynett et  
422 al., 2022). The first oscillation mode of central Chile is centered around ~100 min (Aranguiz et al., 2019).  
423 Consequently, Figure 11 illustrates that the long-lasting tsunami energy of the two events is respectively  
424 distributed in 20–30 min period at East Cape in New Zealand and in ~100 min period at Talcahuaho in  
425 central Chile. The coupling of bathymetric oscillation mode with tsunami containing similar-period wave  
426 results in the excitement of tsunami resonance, which amplifies tsunami waves and prolongs the tsunami  
427 oscillation at the two stations (Heidarzadeh et al., 2019, 2021; Hu et al., 2022; Wang et al., 2022).  
428 Simply put, atmospheric acoustic-gravity waves from the 2022 HTHH eruption do not directly contribute  
429 to the long-lasting tsunami, but the resonance effect associated with ocean waves theoretically could  
430 contribute to it. However, the similarity of far-field hydrodynamic behaviors between the 2022 HTHH  
431 volcanic tsunami and the 2011 Tohoku seismogenic tsunami demonstrates the both went through similar  
432 hydrodynamic processes after their arrivals. The consistency favors that the long-lasting tsunami of 2022  
433 HTHH tsunami event can very likely be attributed by the interplays between local bathymetry and  
434 conventional tsunami left after each passage of atmospheric waves, which can well explain why the two  
435 completely distinct tsunami events possess a comparable duration time.

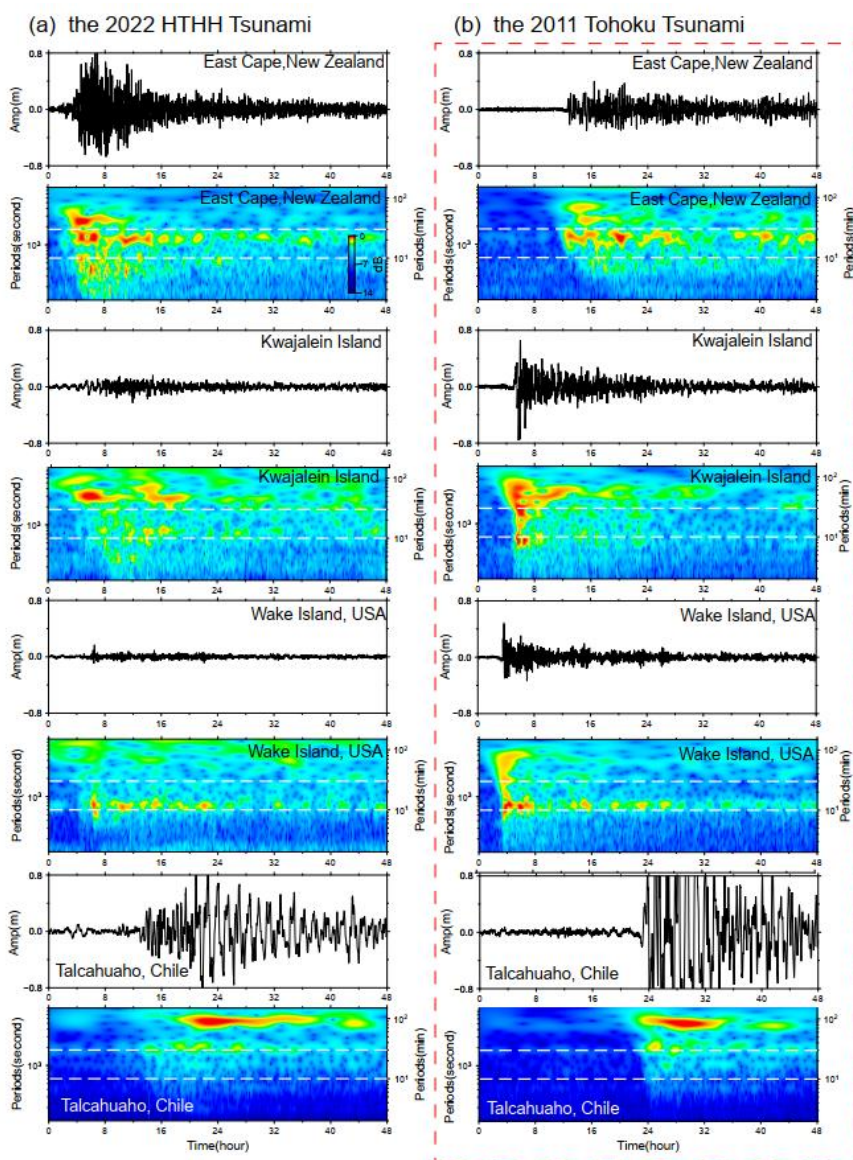


436

437 **Figure 10. Tsunami duration. (a) Tsunami durations at Pacific 116 tide gauges through ARMS level approach.**

438 **(b) the location of barographs (blue curves) and nearby tide gauges (green curves), as well as their waveforms.**

439



440  
441 **Figure 11.** Wavelet analysis of tsunami waveforms recorded by 4 tide gauges during (a) the 2022 HTHH  
442 tsunami event, and (b) the 2011 Tohoku tsunami event.

### 443 4.3 Challenges for Tsunami Warning

444 The generation mechanisms and hydrodynamic characteristics of the 2022 HTHH volcanic tsunami are  
445 more complicated than pure seismogenic tsunami, which challenge the traditional tsunami warning  
446 approach.



447 The first challenge is posed by the tsunami components with propagating velocities faster than the  
448 conventional tsunami. The Tonga volcanic tsunami event provides an excellent example which highlights  
449 that the tsunamigenic mechanisms are not limited to tectonic activities related with the sudden seafloor  
450 displacements, but also include a variety of atmospheric waves with distinct propagation velocities. The  
451 tsunami components in 2022 HTHH event generated by the air-sea coupling possess a wide range of  
452 velocities from 1000 m/s to 200 m/s. The Lamb waves recorded in both the 2022 HTHH event and the  
453 1833 Krakatoa volcanic event traveled along the Earth's surface globally for several times (Carvajal et  
454 al., 2022). The tsunami waves produced by Lamb waves, the wave components associated with resonance  
455 of the air-sea coupling and their superimposition increase the difficulty of tsunami warning.

456 Another critical challenge is associated with the interplays between tsunami waves and local bathymetry.  
457 The tsunami waves left by each passage of the atmospheric waves can interact with local bathymetry at  
458 coastlines, such as continental shelves with different slopes, and harbor/bay with different shapes and  
459 sizes. The interaction can intensify the tsunami impact and excite a variety of natural oscillation periods.  
460 The 2022 HTHH tsunami with an extremely wide period range of ~2–100 min have a great potential to  
461 couple with the excited natural oscillations and form extensive tsunami resonance phenomena. The  
462 resonance effects result in long-lasting oscillation and delayed tsunami wave peaks. The uncertain  
463 arrivals of the maximum tsunami waves pose an extra challenge to tsunami warning.

#### 4645. **Conclusion**

465 In the study, we explore the tsunamigenic mechanisms and the hydrodynamic characteristics of the 2022  
466 HTHH volcanic tsunami event. Through extensive analysis of waveforms recorded by the DART buoys,  
467 tide gauges and barometers in the Pacific Ocean, we reach the main findings as follows:

468 (1) We identify four distinct tsunami wave components based on their distinct propagation velocities or  
469 period bands (~80–100 min, 10–30 min, 30–40 min, and 3–5 min). The generation mechanisms of these  
470 tsunami components range from air-sea coupling to seafloor crustal deformation during the volcanic  
471 eruption.

472 (2) The first-arriving tsunami component with 80–100 min period was most likely from shock wave  
473 spreading at a velocity of ~1000 m/s in the vicinity of the eruption. This tsunami component was not  
474 clearly identified by currently available publication and it's not easy to be visually observed through time



475 series of the waveforms. The physical mechanism is yet to be understood. The second tsunami component  
476 with 30–40 min period was from Lamb waves, and was the most discussed tsunami source of this event  
477 so far. A thorough analysis of DART measurements indicates that the Lamb waves traveled at the speed  
478 of ~340 m/s in the vicinity of the eruption and decreased to ~315 m/s when traveling away due to cooling  
479 of the air temperature. The third tsunami component was from some atmospheric gravity wave modes  
480 with propagation velocity faster than 200 m/s but slower than Lamb waves. The last tsunami component  
481 with the shortest periods 3–5 min was probably produced by partial caldera collapse with estimated  
482 dimension of ~0.8–1.8 km.

483 (3) The long-lasting Pacific oscillation of this tsunami event was not only associated with the resonance  
484 effect with the atmospheric acoustic-gravity waves, but more importantly the interactions with local  
485 bathymetry. The velocities of tsunami waves in deep ocean (especially at Mariana and Tonga-Kermadec  
486 trenches) close to those of acoustic Lamb waves and some gravity wave modes produced resonance  
487 effects, which supplied energy to the ocean. The comparison of hydrodynamical characteristics between  
488 the 2022 HTHH tsunami event and the 2011 Tohoku tsunami event suggests the volcanic tsunami  
489 oscillation was prolonged by their interplays with local bathymetry.

490 (4) The extraordinary features of this rare volcanic tsunami event challenge the current tsunami warning  
491 system which is mainly designed for seismogenic tsunamis. It is necessary to improve the awareness of  
492 people at risks about the potential tsunami hazards associated with volcanic eruptions. New approaches  
493 are expected to be developed for tsunami hazard assessments with these unusual sources: various  
494 atmospheric waves radiated by volcanic eruptions besides those traditionally recognized, e.g.  
495 earthquakes, landslides, caldera collapses and pyroclastic flows etc.

#### 496 **Acknowledgment**

497 This work was supported by National Natural Science Foundation (No 41976197, No 12002099),  
498 Innovation Group Project of Southern Marine Science and Engineering Guangdong Laboratory (Zhuhai)  
499 (No. 311021002), Key Research and Development Program of Hainan Province (No. ZDYF2020209),  
500 Southern Marine Science and Engineering Guangdong Laboratory (Zhuhai) (SML2021SP305) and  
501 Fundamental Research Funds for the Central Universities, Sun Yat-sen University (2021qntd23).

502 The JAGURS tsunami simulation code is employed for tsunami modelling (Baba et al., 2015;





503 <https://zenodo.org/record/6118212#.Yk98qdtBxPY>). Bathymetry data are obtained from GEBCO at  
504 <http://www.gebco.net>. The sea level records in deep ocean are available from the Deep Ocean Assessment  
505 and Reporting of Tsunamis (DART) buoy network in the Pacific (<https://nctr.pmel.noaa.gov/Dart/>), and  
506 GeoNet New Zealand DART network (<https://tilde.geonet.org.nz>). The sea level records of tide gauges  
507 are downloaded from UNESCO/ IOC (<http://www.ioc-sealevelmonitoring.org/>). Barometer data are  
508 provided by the following providers: Direcció'n Meteorol'gica de Chile  
509 (<https://climatologia.meteochile.gob.cl>), NOAA National Weather Service  
510 (<https://www.weather.gov/ilm/observations>), Japan Meteorological Agency (<https://www.jma.go.jp>),  
511 The UK Met Office Weather Observation (<https://www.metoffice.gov.uk/observations>), and Fiji  
512 Meteorological Service (<https://www.met.gov.fj>).

#### 513 Reference

- 514 Adam, D.: Tonga volcano created puzzling atmospheric ripples, *Nature*,  
515 <https://doi.org/10.1038/d41586-022-00127-1>, 2022.
- 516 Amores, A., Monserrat, S., Marcos, M., Argüeso, D., Villalonga, J., Jordà, G., and Gomis, D.:  
517 Numerical simulation of atmospheric Lamb waves generated by the 2022 Hunga-Tonga volcanic  
518 eruption, *Geophys. Res. Lett.*, 49, e2022GL098240, <https://doi.org/10.1029/2022GL098240>, 2022.
- 519 Aranguiz, R., Catalán, P. A., Cecioni, C., Bellotti, G., Henriquez, P., and González, J.: Tsunami  
520 Resonance and Spatial Pattern of Natural Oscillation Modes With Multiple Resonators, *J. Geophys.*  
521 *Res. Ocean.*, 124, 7797–7816, <https://doi.org/10.1029/2019JC015206>, 2019.
- 522 Baba, T., Takahashi, N., Kaneda, Y., Ando, K., Matsuoka, D., and Kato, T.: Parallel Implementation of  
523 Dispersive Tsunami Wave Modeling with a Nesting Algorithm for the 2011 Tohoku Tsunami, *Pure*  
524 *Appl. Geophys.*, 172, 3455–3472, <https://doi.org/10.1007/s00024-015-1049-2>, 2015.
- 525 Bevis, M., Taylor, F. W., Schutz, B. E., Recy, J., Isacks, B. L., Helu, S., Singh, R., Kendrick, E.,  
526 Stowell, J., Taylor, B., and Calmantli, S.: Geodetic observations of very rapid convergence and back-  
527 arc extension at the tonga arc, *Nature*, 374, 249–251, <https://doi.org/10.1038/374249a0>, 1995.
- 528 Billen, M. I., Gurnis, M., and Simons, M.: Multiscale dynamics of the Tonga–Kermadec subduction  
529 zone, *Geophys. J. Int.*, 153, 359–388, <https://doi.org/10.1046/j.1365-246X.2003.01915.x>, 2003, 2003.
- 530 Carvajal, M., Sepúlveda, I., Gubler, A., and Garreaud, R.: Worldwide Signature of the 2022 Tonga



- 531 Volcanic Tsunami, *Geophys. Res. Lett.*, 49, e2022GL098153, <https://doi.org/10.1029/2022GL098153>,  
532 2022.
- 533 Duncombe, J.: The Surprising Reach of Tonga's Giant Atmospheric Waves.pdf, *Eos (Washington*  
534 *DC)*., 103, <https://doi.org/10.1029/2022EO220050>, 2022.
- 535 Edmonds, M.: Hunga-Tonga-Hunga-Ha'apai in the south Pacific erupts violently, *Temblor*,  
536 <https://doi.org/10.32858/temblor.231>, 2022.
- 537 Garvin, J. B., Slayback, D. A., Ferrini, V., Frawley, J., Giguere, C., Asrar, G. R., and Andersen, K.:  
538 Monitoring and Modeling the Rapid Evolution of Earth's Newest Volcanic Island: Hunga Tonga  
539 Hunga Ha'apai (Tonga) Using High Spatial Resolution Satellite Observations, *Geophys. Res. Lett.*, 45,  
540 3445–3452, <https://doi.org/10.1002/2017GL076621>, 2018.
- 541 Gossard, E. E. and Hooke, W. H.: *Waves in the Atmosphere*, Amsterdam: Elsevier, 1975.
- 542 Heidarzadeh, M. and Satake, K.: Waveform and Spectral Analyses of the 2011 Japan Tsunami Records  
543 on Tide Gauge and DART Stations Across the Pacific Ocean, *Pure Appl. Geophys.*, 170, 1275–1293,  
544 <https://doi.org/10.1007/s00024-012-0558-5>, 2013.
- 545 Heidarzadeh, M. and Satake, K.: Excitation of Basin-Wide Modes of the Pacific Ocean Following the  
546 March 2011 Tohoku Tsunami, *Pure Appl. Geophys.*, 171, 3405–3419, [https://doi.org/10.1007/s00024-](https://doi.org/10.1007/s00024-013-0731-5)  
547 [013-0731-5](https://doi.org/10.1007/s00024-013-0731-5), 2014.
- 548 Hu, G., Feng, W., Wang, Y., Li, L., He, X., Karakaş, Ç., and Tian, Y.: Source characteristics and  
549 exacerbated tsunami hazard of the 2020 Mw 6.9 Samos earthquake in eastern Aegean Sea, *J. Geophys.*  
550 *Res. Solid Earth*, 127, e2022JB023961, <https://doi.org/10.1029/2022JB023961>, 2022.
- 551 Kawata, Y., Benson, B. C., Borrero, J. C., Borrero, J. L., Davies, H. L., Lange, W. P. de, Imamura, F.,  
552 Letz, H., Nott, J., and Synolakis, C. E.: Tsunami in Papua New Guinea Was as Intense as First  
553 Thought, *Eos, Trans. Am. Geophys. Union*, 80, 9, <https://doi.org/10.1029/99EO00065>, 1999.
- 554 Kristeková, M., Kristek, J., Moczo, P., and Day, S. M.: Misfit Criteria for Quantitative Comparison of  
555 Seismograms, *Bull. Seismol. Soc. Am.*, 96, 1836–1850, <https://doi.org/10.1785/0120060012>, 2006.
- 556 Kubota, T., Saito, T., and Nishida, K.: Global fast-traveling tsunamis by atmospheric pressure waves  
557 on the 2022 Tonga eruption, *Science (80-. )*., <https://doi.org/10.1126/science.abo4364>, 2022.
- 558 Kulichkov, S. N., Chunchuzov, I. P., Popov, O. E., Gorchakov, G. I., Mishenin, A. A., Perepelkin, V.  
559 G., Bush, G. A., Skorokhod, A. I., Yu. A. Vinogradov, Semutnikova, E. G., Šepic, J., Medvedev, I. P.,



- 560 Gushchin, R. A., Kopeikin, V. M., Belikov, I. B., Gubanova, D. P., and A. V. Karpov & A. V.  
561 Tikhonov: Acoustic-Gravity Lamb Waves from the Eruption of the Hunga-Tonga-Hunga-Hapai  
562 Volcano, Its Energy Release and Impact on Aerosol Concentrations and Tsunami, *Pure Appl.*  
563 *Geophys.*, <https://doi.org/10.1007/s00024-022-03046-4>, 2022.
- 564 De Lange, W. P. and Healy, T. R.: New Zealand tsunamis 1840–1982, *New Zeal. J. Geol. Geophys.*,  
565 29, 115–134, <https://doi.org/10.1080/00288306.1986.10427527>, 1986.
- 566 Lin, J., Rajesh, P. K., Lin, C. C. H., Chou, M., Liu, J.-Y., Yue, J., Hsiao, T.-Y., Tsai, H.-F., Chao, H.-  
567 M., and Kung, M.-M.: Rapid Conjugate Appearance of the Giant Ionospheric Lamb Wave Signatures  
568 in the Northern Hemisphere After Hunga- Tonga Volcano Eruptions, *Geophys. Res. Lett.*, 49,  
569 e2022GL098222, <https://doi.org/10.1029/2022GL098222>, 2022.
- 570 Liu, P. L.-F. and Higuera, P.: Water waves generated by moving atmospheric pressure : Theoretical  
571 analyses with applications to the 2022 Tonga event, *arXiv Prepr.*,  
572 <https://doi.org/10.48550/arXiv.2205.05856>, 2022.
- 573 Liu, X., Xu, J., Yue, J., and Kogure, M.: Strong Gravity Waves Associated With Tonga Volcano  
574 Eruption Revealed by SABER Observations, *Geophys. Res. Lett.*, 49, e2022GL098339,  
575 <https://doi.org/10.1029/2022GL098339>, 2022.
- 576 Lynett, P., McCann, M., Zhou, Z., Renteria, W., Borrero, J., Greer, D., Fa’anunu, ‘Ofa, Bosserelle, C.,  
577 Jaffe, B., Selle, S. La, Ritchie, A., Snyder, A., Nasr, B., Bott, J., Graehl, N., Synolakis, C., Ebrahimi,  
578 B., and Cinar, E.: The Tsunamis Generated by the Hunga Tonga- Hunga Ha ’apai Volcano on January  
579 15 , 2022, *ResearchSquare*, <https://doi.org/10.21203/rs.3.rs-1377508/v1>, 2022.
- 580 Matoza, R. S., Matoza, R. S., Fee, D., Assink, J. D., Iezzi, A. M., Green, D. N., Kim, K., Lecocq, T.,  
581 Krishnamoorthy, S., Lalande, J., Nishida, K., and Gee, K. L.: Atmospheric waves and global  
582 seismoacoustic observations of the January 2022 Hunga eruption ,*Tonga, Science* (80- ),  
583 <https://doi.org/10.1126/science.abo7063>, 2022.
- 584 Mori, N., Takahashi, T., Yasuda, T., and Yanagisawa, H.: Survey of 2011 Tohoku earthquake tsunami  
585 inundation and run-up, *Geophys. Res. Lett.*, 38, L00G14, <https://doi.org/10.1029/2011GL049210>,  
586 2011.
- 587 NASA: National Aeronautics and Space Administration, “Dramatic changes at Hunga Tonga-Hunga  
588 Ha’apai,” 2022.



- 589 Nomanbhoy, N. and Satake, K.: Generation mechanism of tsunamis from the 1883 Krakatau Eruption,  
590 *Geophys. Res. Lett.*, 22, 509–512, <https://doi.org/10.1029/94GL03219>, 1995.
- 591 Omira, R., Baptista, M. A., Quartau, R., Ramalho, R. S., Kim, J., Ramalho, I., and Rodrigues, A.: How  
592 hazardous are tsunamis triggered by small-scale mass-wasting events on volcanic islands ? New  
593 insights from Madeira–NE Atlantic, *Earth Planet. Sci. Lett.*, 578, 117333,  
594 <https://doi.org/10.1016/j.epsl.2021.117333>, 2022.
- 595 Otsuka, S.: Visualizing Lamb Waves From a Volcanic Eruption Using Meteorological Satellite  
596 Himawari-8, *Geophys. Res. Lett.*, 49, e2022GL098324, <https://doi.org/10.1029/2022GL098324>, 2022.
- 597 Pelinovsky, E., Choi, B. H., Stromkov, A., Didenkulova, I., and Kim, H.: Analysis of Tide-Gauge  
598 Records of the 1883 Krakatau Tsunami. In: Satake, K. (eds) *Tsunamis*, *Adv. Nat. Technol. Hazards*  
599 *Res.*, 23, Springer, Dordrech, [https://doi.org/10.1007/1-4020-3331-1\\_4](https://doi.org/10.1007/1-4020-3331-1_4), 2005.
- 600 Plank, S., Marchese, F., Genzano, N., Nolde, M., and Martinis, S.: The short life of the volcanic island  
601 New Late`iki (Tonga) analyzed by multi-sensor remote sensing data, *Sci. Rep.*, 10, 22293,  
602 <https://doi.org/10.1038/s41598-020-79261-7>, 2020.
- 603 Rabinovich, A. B.: Seiches and harbor oscillations. in: *Handbook of coastal and ocean engineering*, pp,  
604 193–236, 2009.
- 605 Rabinovich, A. B., Thomson, Æ. R. E., and Stephenson, F. E.: The Sumatra tsunami of 26 December  
606 2004 as observed in the North Pacific and North Atlantic oceans, *Surv. Geophys.*, 27, 647–677,  
607 <https://doi.org/10.1007/s10712-006-9000-9>, 2006.
- 608 Rabinovich, A. B., Titov, V. V., Moore, C. W., and Eble, M. C.: The 2004 Sumatra Tsunami in the  
609 Southeastern Pacific Ocean: New Global Insight From Observations and Modeling, *J. Geophys. Res.*  
610 *Ocean.*, 122, 7992–8019, <https://doi.org/https://doi.org/10.1002/2017JC013078>, 2017.
- 611 Ramalho, R. S., Winckler, G., Madeira, J., Helffrich, G. R., Hipólito, A., Quartau, R., Adena, K., and  
612 Schaefer, J. M.: Hazard potential of volcanic flank collapses raised by new megatsunami evidence, *Sci.*  
613 *Adv.*, 1, e1500456, <https://doi.org/10.1126/sciadv.1500456>, 2015.
- 614 Ramírez-Herrera, M. T., Coca, O., and Vargas-Espinosa, V.: Tsunami Effects on the Coast of Mexico  
615 by the Hunga Tonga-Hunga Ha`apai Volcano, *Pure Appl. Geophys.*, [https://doi.org/10.1007/s00024-](https://doi.org/10.1007/s00024-022-03017-9)  
616 [022-03017-9](https://doi.org/10.1007/s00024-022-03017-9), 2022.
- 617 Satake, K.: Earthquakes: Double trouble at Tonga, *Nature*, 466, 931–932,



- 618 <https://doi.org/10.1038/466931a>, 2010.
- 619 Satake, K., Heidarzadeh, M., Quiroz, M., and Cienfuegos, R.: History and features of trans-oceanic  
620 tsunamis and implications for paleo-tsunami studies, *Earth-Science Rev.*, 202, 103112,  
621 <https://doi.org/10.1016/j.earscirev.2020.103112>, 2020.
- 622 Self, S. and Rampino, M. R.: K-1981Self\_Nature\_The 1883 eruption of Krakatau, *Nature*, 294, 699–  
623 704, <https://doi.org/10.1038/294699a0>, 1981.
- 624 Stern, S., Cronin, S., Ribo, M., Barker, S., Brenna, M., Smith, I. E. M., Ford, M., Kula, T., and  
625 Vaiomounga, R.: Post-2015 caldera morphology of the Hunga Tonga-Hunga Ha 'apai caldera ,  
626 Tonga , through drone photogrammetry and summit area bathymetry, *EGU Gen. Assem.* 2022,  
627 <https://doi.org/10.5194/egusphere-egu22-13586>, 2022.
- 628 Tanioka, Y., Yamanaka, Y., and Nakagaki, T.: Characteristics of the deep sea tsunami excited offshore  
629 Japan due to the air wave from the 2022 Tonga eruption, *Earth, Planets Sp.*, 74, 61,  
630 <https://doi.org/10.1186/s40623-022-01614-5>, 2022.
- 631 Themens, D. R., Watson, C., Žagar, N., Vasylykevych, S., Elvidge, S., McCaffrey, A., Prikryl, P., Reid,  
632 B., Wood, A., and Jayachandran, P. T.: Global Propagation of Ionospheric Disturbances Associated  
633 With the 2022 Tonga Volcanic Eruption, *Geophys. Res. Lett.*, 49, e2022GL098158,  
634 <https://doi.org/10.1029/2022GL098158>, 2022.
- 635 Titov, V., Rabinovich, A. B., Mofjeld, H. O., Thomson, R. E., and Gonza, F. I.: The Global Reach of  
636 the 26 December 2004 Sumatra Tsunami, *Science (80-. )*, 309, 2045–2049,  
637 <https://doi.org/10.1126/science.1114576>, 2005.
- 638 USGS: M 5.8 Volcanic Eruption - 68 km NNW of Nuku'alofa, Tonga, *U.S. Geol. Surv.*, 2022.
- 639 Wang, Y., Heidarzadeh, M., Satake, K., Mulia, I. E., and Yamada, M.: A Tsunami Warning System  
640 Based on Offshore Bottom Pressure Gauges and Data Assimilation for Crete Island in the Eastern  
641 Mediterranean Basin, *J. Geophys. Res. Solid Earth*, 125, e2020JB020293,  
642 <https://doi.org/10.1029/2020JB020293>, 2020.
- 643 Wang, Y., Zamora, N., Quiroz, M., Satake, K., and Cienfuegos, R.: Tsunami Resonance  
644 Characterization in Japan Due to Trans-Pacific Sources: Response on the Bay and Continental Shelf, *J.*  
645 *Geophys. Res. Ocean.*, 126, 1–16, <https://doi.org/10.1029/2020JC017037>, 2021.
- 646 Wang, Y., Heidarzadeh, M., Satake, K., and Hu, G.: Characteristics of two tsunamis generated by



647 successive Mw 7.4 and Mw 8.1 earthquakes in Kermadec Islands on March 4,2021, Nat. Hazards Earth  
648 Syst. Sci., 22, 1–10, <https://doi.org/10.5194/nhess-2021-369>, 2022.

649 Yuen, D. A., Scruggs, M. A., Spera, F. J., Yingcai Zheng, Hao Hu, McNutt, S. R., Glenn Thompson,  
650 Mandli, K., Keller, B. R., Wei, S. S., Peng, Z., Zhou, Z., Mulargia, F., and Tanioka1, Y.: Under the  
651 Surface: Pressure-Induced Planetary-Scale Waves, Volcanic Lightning, and Gaseous Clouds Caused by  
652 the Submarine Eruption of Hunga Tonga-Hunga Ha’apai Volcano Provide an Excellent Research  
653 Opportunity, Earthq. Res. Adv., <https://doi.org/10.1016/j.eqrea.2022.100134>, 2022.

654 Zhang, S., Vierinen, J., Aa, E., Goncharenko, L. P., Erickson, P. J., Rideout, W., Coster, A. J., and  
655 Spicher, A.: 2022 Tonga Volcanic Eruption Induced Global Propagation of Ionospheric Disturbances  
656 via Lamb Waves, Front. Astron. Sp. Sci., 9, 1–10, <https://doi.org/10.3389/fspas.2022.871275>, 2022.  
657